Materials Horizons

ROYAL SOCIETY OF CHEMISTRY

COMMUNICATION

View Article Online
View Journal

Cite this: DOI: 10.1039/d6mh00184j

Received 30th January 2026,
Accepted 30th March 2026

DOI: 10.1039/d6mh00184j

rsc.li/materials-horizons

High-entropy layered oxide electrocatalyst derived from spent battery cathodes for overall water splitting and 2,5 hydroxymethylfurfural (HMF) oxidation

Angga Hermawan, *[a] Ula Miftakhun Nikmah,[b] Angga Dito Fauzi,[b] Sri Rahayu,[c] Andri Hardiansyah,[a] Ni Luh Wulan Septiani, [d] Hismiaty Bahua,[e] Indri Badria Adilina,[f] Maykel T. E. Manawan,[f] Munawar Khalil, [g] Andrea Zitolo,[h] Aniruddha Deb,[h] Mathieu Prevot [i] and Lydia Helena Wong *[j]

The rapid expansion of lithium-ion battery (LIB) use has led to a critical waste management challenge, with end-of-life cells contributing to environmental degradation and resource depletion. Here, we report a low-temperature (100 °C) synthesis of high-entropy layered oxides, $Li_xNa_{1-x}(NiCoMnFe)O_2$, directly upcycled from spent LIB cathodes. These materials were designed and optimized as trifunctional electrocatalysts for overall water splitting (HER and OER) and 5-hydroxymethylfurfural (HMF) oxidation. Systematic compositional tuning revealed that the Ni-rich variant outperforms its counterparts, achieving overpotentials of 434 mV for the HER and 310 mV for the OER at 10 mA cm^{-2}, with corresponding Tafel slopes of 113 and 81 mV dec^{-1}, approaching the performance of Pt/C and RuO_2 benchmarks, respectively. Simultaneously, this catalyst facilitates the selective electrooxidation of HMF to 2,5-furandicarboxylic acid (FDCA), achieving an FE of about 18% for FDCA and around 64% for hydrogen during co-electrolysis. The catalyst retains activity over 16 h during flow-cell operation. A cradle-to-gate life-cycle assessment shows that allocating environmental impacts to FDCA as a co-product reduces impacts relative to a hydrogen-only pathway. Moreover, as the electricity source is the dominant source of CO_2 footprint, switching to renewable grids can lower the global warming potential (GWP, in Kg CO_2-eq) by ≈80%. Our work offers a scalable, energy-efficient platform that integrates LIB waste remediation with renewable hydrogen generation and biomass upgrading.

New concepts

We present a low-temperature, scalable strategy to upcycle spent lithium-ion battery cathodes into high-entropy layered oxide electrocatalysts active for the HER, OER, and HMF oxidation. By bypassing high-temperature annealing and directly using leachates from battery waste, our approach minimizes energy input and resource use. The Ni-rich catalyst achieves bifunctional water splitting performance near that of noble metals and enables co-electrolysis of HMF and water to produce hydrogen and value-added chemicals simultaneously. This work pioneers a circular-economy strategy for high-performance electrocatalyst production, transforming LIB waste into next-generation, high-entropy materials for clean-energy technologies.

Introduction

Lithium-ion batteries (LIBs) have revolutionized portable electronics and are now at the forefront of the electric-vehicle (EV) transition, supporting the development of clean and sustainable energy systems worldwide.[1–3] However, the rapid growth in EV deployment, from 2.1 million units in 2018 to 13.7 million in 2023, has created an urgent challenge: end-of-life LIB waste is projected to exceed 11 000 tons by 2030, yet under 5% of this volume is currently recycled.[4–6] If this situation is left unmanaged, these discarded cells threaten to become a significant environmental burden, leaching transition-metal ions into

[a] Research Center for Nanotechnology System, National Research and Innovation Agency (BRIN), South Tangerang, Banten, 15314, Indonesia. E-mail: angga.hermawan@brin.go.id
[b] Department of Physics, Faculty of Science and Technology, Universitas Airlangga, Kampus Merr C, Jl. Dr Ir. H. Soekarno, Mulyorejo, Surabaya, 60115, Indonesia
[c] Research Center for Fuel Technology, National Research and Innovation Agency (BRIN), South Tangerang, Banten, 15314, Indonesia
[d] Research Center for Electronic, National Research and Innovation Agency (BRIN), Bandung, West Java, 40132, Indonesia
[e] Research Center for Sustainable Industrial and Manufacturing Systems, National Research and Innovation Agency (BRIN), South Tangerang, Banten, 15314, Indonesia
[f] Research Center for Catalysis, National Research and Innovation Agency (BRIN), South Tangerang, Banten, 15314, Indonesia
[g] Department of Chemistry, Faculty of Mathematics and Natural Sciences, University of Indonesia, Depok, 16424, Indonesia
[h] Sigray Inc., 5500 E 2nd Street, Benicia, CA, 94510, USA
[i] Université Claude Bernard Lyon 1, CNRS, IRCELYON UMR 5256, Villeurbanne, F-69100, France
[j] School of Material Science and Engineering, Nanyang Technological University, Singapore, 639798, Singapore. E-mail: lydiawong@ntu.edu.sg

ecosystems and contributing to resource depletion. The crucial point of this recycling challenge lies in the complex cathode architecture, typically layered oxides of nickel, cobalt, manganese, and sometimes iron (Ni–Co–Mn–Fe), whose crystal structures become damaged during repeated charge–discharge cycles.[5,6] Although several recycling schemes recover these metals, the recycled products often exhibit degraded crystal structures, residual impurities, and diminished electrochemical performance compared with virgin materials.[5,7,8] Given these limitations, a paradigm shift is needed: rather than attempting to restore spent cathode materials to battery-grade purity, we can revalorize them directly as electrocatalysts. This approach leverages the intrinsic redox chemistry of Ni, Co, Mn, and Fe to drive reactions that underpin renewable-energy technologies, most notably, the electrochemical water-splitting reactions that produce green hydrogen.[1,6]

Electrochemical water splitting (EWS) is a cornerstone technology for sustainable hydrogen production. Nevertheless, its practical deployment is hindered by the sluggish kinetics and high overpotentials of the oxygen-evolution reaction (OER), which involves a four-electron transfer, and the dual-electron hydrogen-evolution reaction (HER). Overpotentials in excess of the thermodynamic 1.23 V threshold translate directly into increased energy consumption and diminished system efficiency.[9–11] Catalysts are therefore essential to lower these energy barriers, stabilize reaction intermediates, and enhance charge transfer. Although noble-metal catalysts (*e.g.*, Pt/C for the HER, Ir/Ru oxides for the OER) remain state-of-the-art, their scarcity and cost are concerns with regards to large-scale deployment and long-term sustainability.[9–11] Transition-metal oxides, particularly nickel-rich composites ($NiFeO_2$, $NiCoO_2$, *etc.*), have emerged as promising alternatives, but their synthesis frequently relies on high-purity precursors and energy-intensive heat treatments.[12]

Moreover, the emerging field of biomass-derived electrosynthesis highlights the advantage of coupling hydrogen evolution at the cathode with oxidation of biomass-derived organics at the anode. In particular, 5-hydroxymethylfurfural (HMF) is a platform molecule derived from carbohydrate feedstocks. It can be electrooxidized to 2,5-furandicarboxylic acid (FDCA) or 2-furancarboxylic acid (FCA), key monomers for bio-based polymers, under milder conditions and at lower potentials than water oxidation.[13–16] Co-electrolyzing HMF with water is an attractive pathway not only to improve process economics but also to reduce overall environmental impacts compared to running separate water- and biomass-electrolysis processes. Fortunately, transition-metal catalysts, especially nickel-containing materials, have proven to be excellent electrocatalysts for the HER, OER and HMF oxidation.[17–22] Such trifunctional catalysts enable an integrated, economically attractive route to simultaneous clean hydrogen production and value-added chemical synthesis.

There have been several reports of repurposing spent lithium-ion battery cathodes as electrocatalysts. In our previous study we demonstrated that NiCoMnFe layered double hydroxides (LDHs) derived from these cathodes exhibited OER activity with an overpotential of 329 mV and stable operation over 10 h.[23] Similar LDHs, such as α-$Co(OH)_2$ and $Ni_{0.5}Mn_{0.3}Co_{0.2}(OH)_2$ have also been successfully fabricated from spent cathodes and shown strong OER performance.[24,25] Cobalt nitride catalysts derived from battery waste have been demonstrated to have bifunctional activity for both the HER and OER.[26] Although such catalysts show promise for hydrogen production, they have not been demonstrated for HMF oxidation. Recently, high-entropy materials have emerged as a novel class of electrocatalysts for energy-related applications.[27–29] High-entropy oxides (HEOs), which integrate five or more metal cations that sit within the same crystallographic site, offer structural complexity, tunable electronic properties and potential synergistic interactions among constituent metals. Several HEOs exhibit exceptional promise as electrocatalysts for the OER, the critical anodic half-reaction in the nitrogen reduction reaction (NRR), water splitting, and CO_2 reduction reaction (CO_2RR).[30–32] However, conventional HEO synthesis typically requires temperatures above 600 °C and high-purity metal salts, posing challenges for scalability and sustainability.[33,34] To date, no studies have reported the low-temperature, direct conversion of lithium-ion battery cathode leachates into HEO electrocatalysts, nor have systematic investigations that correlate their elemental composition with trifunctional activity for the HER, OER, and HMF oxidation.

Here, we report a low-temperature (100 °C) synthesis of $Li_xNa_{1-x}(NiCoMnFe)O_2$ high-entropy layered oxide catalysts, directly derived from spent LIB cathodes. Transition metal ions were recovered *via* acid leaching and subsequently processed through a facile co-precipitation method, yielding single-phase layered oxides without the need for high-temperature annealing typically required in conventional routes (see the SI for details of the experiment). By systematically varying the Ni, Co, Mn, and Fe ratios in $Li_xNa_{1-x}(NiCoMnFe)O_2$, we identified a Ni-rich composition that optimally lowers the overpotentials for the HER, OER and HMF electrooxidation. The optimized catalyst enables HMF oxidation potentials lower than water oxidation, while simultaneously driving hydrogen production at the cathode with a faradaic efficiency of 64% for the HER and over 18% for FDCA formation under co-electrolysis conditions. Notably, the catalyst exhibits excellent stability, maintaining performance for over 16 h in a flow-electrolyzer configuration. The systematic characterizations have correlated the structure–activity relationship. This trifunctional catalyst design, achieved *via* battery waste valorization and low-energy synthesis, offers a sustainable alternative to conventional electrocatalysts by integrating clean hydrogen production with biomass upgrading. Complementary life-cycle assessment further confirms the environmental benefits of this approach, showing that allocating impacts to FDCA as a co-product reduces the overall footprint compared with hydrogen-only production.

Results and discussion

The leaching efficiency investigation (Table S1) using ICP-OES indicates that the optimum H_2O_2 dosage is 1.7 wt%, and

increasing the dosage does not meaningfully improve Ni/Co/Mn/Fe/Li leaching. This is because H_2O_2 primarily serves as a reductant to promote dissolution of the metal oxide. Once sufficient reductant is present, extra H_2O_2 provides little benefit and may be consumed by decomposition/side reactions rather than further leaching.[35] The calculated configurational mixing entropy (ΔS_{mix}, in Table S2) for all samples ranges from 1.52R to 1.61R (12.61–13.36 J mol^{-1} K^{-1}), exceeding the high-entropy threshold of 1.5R and confirming their classification as high-entropy layered oxides.

X-ray diffraction (Fig. 1(a)) indicates that the synthesized materials predominantly crystallize in the α-$NaFeO_2$-type rhombohedral structure (space group $R\bar{3}m$), characteristic of an O3-type layered oxide. The structural schematic in Fig. 1(b) illustrates the expected cation arrangement, where transition-metal ions occupy octahedral 3b sites and Li/Na occupy octahedral 3a sites, forming alternating TMO_6 slabs and alkali (Li/NaO_6) layers within a cubic close-packed oxide framework.[26] Notably, the diffraction peaks are broadened, consistent with the semi-crystalline nature expected from the low synthesis temperature (100 °C) and indicative of limited long-range ordering and/or stacking disorder along the *c*-axis. Weak additional peaks at 2θ around 30–40° are assigned to a secondary $NaMnO_2$ phase. The presence of this minor secondary phase may also suppress coherent crystalline domain growth, which is consistent with the observed broadening.

Upon enriching the parent $Li_xNa_{1-x}NiCoMnFeO_2$ with Fe, Mn, Co, or Ni using a commercial metal nitrate salt (see the SI for details of the experimental procedures), the (003) reflection systematically shifts to higher 2θ (from 19.3° for the pristine sample to 19.45° for other samples), implying contraction of the inter slab (O–Li/Na–O) spacing and a composition-dependent adjustment of the layered lattice. This trend is consistent with the decreasing high-spin ionic radii of Fe^{2+} (0.78 Å), Mn^{2+} (0.67 Å), Co^{2+} (0.65 Å), and Ni^{2+} (0.60 Å), which leads to contraction of the average transition-metal–oxygen framework and modification of the slab/interlayer spacing.[28,36–40] In addition, Fe- and Ni-rich samples show a clearer shift of the (104) peak (from 44.05° to 44.29°), suggesting shorter average TM–O bond lengths and strengthened TM–O interactions. In contrast, the Mn-rich composition exhibits broad peaks at ~14° and ~24°, assigned to the $NaMnO_2$ phase, and shows minimal (104) displacement due to this partial phase segregation.[29–31] Importantly, because waste-derived precursors and low-temperature processing can introduce small fractions of secondary phases below or near the XRD detection limit, the XRD conclusions will be interpreted together with the following complementary characterization to support that the targeted layered high-entropy oxide is the dominant phase, while explicitly acknowledging and assigning the observed minor impurity-related reflections.

Raman spectroscopy was employed to probe the local structure of these high-entropy layered oxides (Fig. 1(c)). Factor-group analysis for the $R\bar{3}m$ (D_3d^5) space group predicts vibrational modes according to the irreducible vibrational modes: $\Gamma = A_{1g} + E_g + 2A_{2u} + 2E_u$, where the A_{1g} and E_g modes are Raman-active, and the $2A_{2u} + 2E_u$ modes are infrared-active.[41,42] Gaussian deconvolution of the Raman spectra reveals an E_g mode near 500 cm^{-1}, corresponding to O–TM–O bending along the *c*-axis, and an A_{1g} mode near 600 cm^{-1}, corresponding to TM–O stretching within the TMO_6 octahedra along the *a*-axis.[43,44] A systematic blue shift of the A_{1g} band is observed in Mn- and Ni-rich samples, consistent with enhanced TM–O bond strength inferred from XRD. It should be noted that, in non-ideal materials, such as those exhibiting non-stoichiometry, additional Raman bands, shifts in peak wavenumbers, and/or band broadening may occur. Notably, an emergent band at approximately 660 cm^{-1} is tentatively ascribed to a pronounced shortening of certain Na–O bonds relative to those in ideal $Li_xNa_{1-x}NiCoMnFeO_2$ layered oxides.[45]

To probe the transition-metal oxidation states and local coordination, we performed *ex situ* X-ray absorption spectroscopy

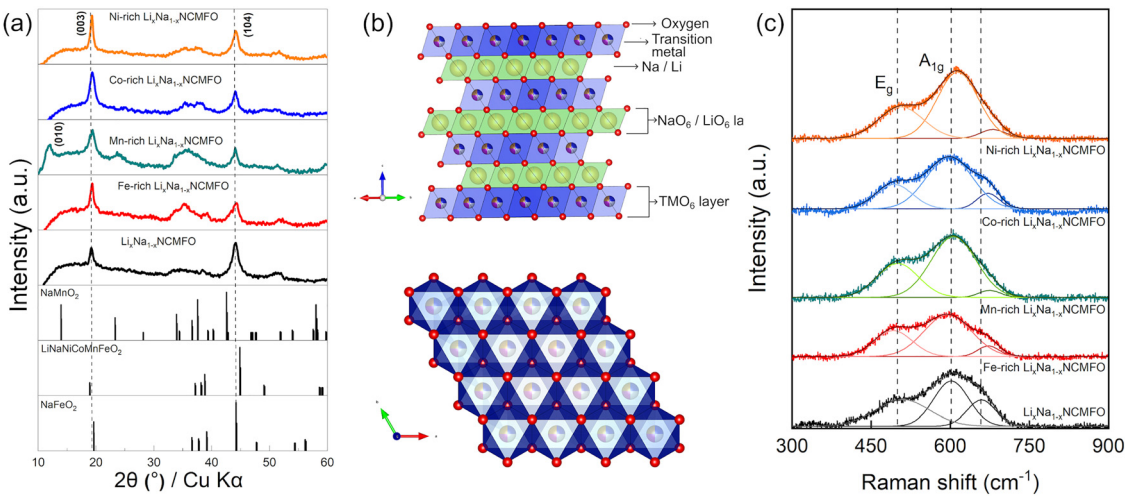

Fig. 1 (a) XRD patterns, (b) representative crystal-structure models (created by VESTA), and (c) Raman spectra of the $Li_xNa_{1-x}NCMFO$, Fe-rich $Li_xNa_{1-x}NCMFO$, Mn-rich $Li_xNa_{1-x}NCMFO$, Co-rich $Li_xNa_{1-x}NCMFO$, and Ni-rich $Li_xNa_{1-x}NCMFO$. Raman spectra were deconvoluted by Gaussian fitting.

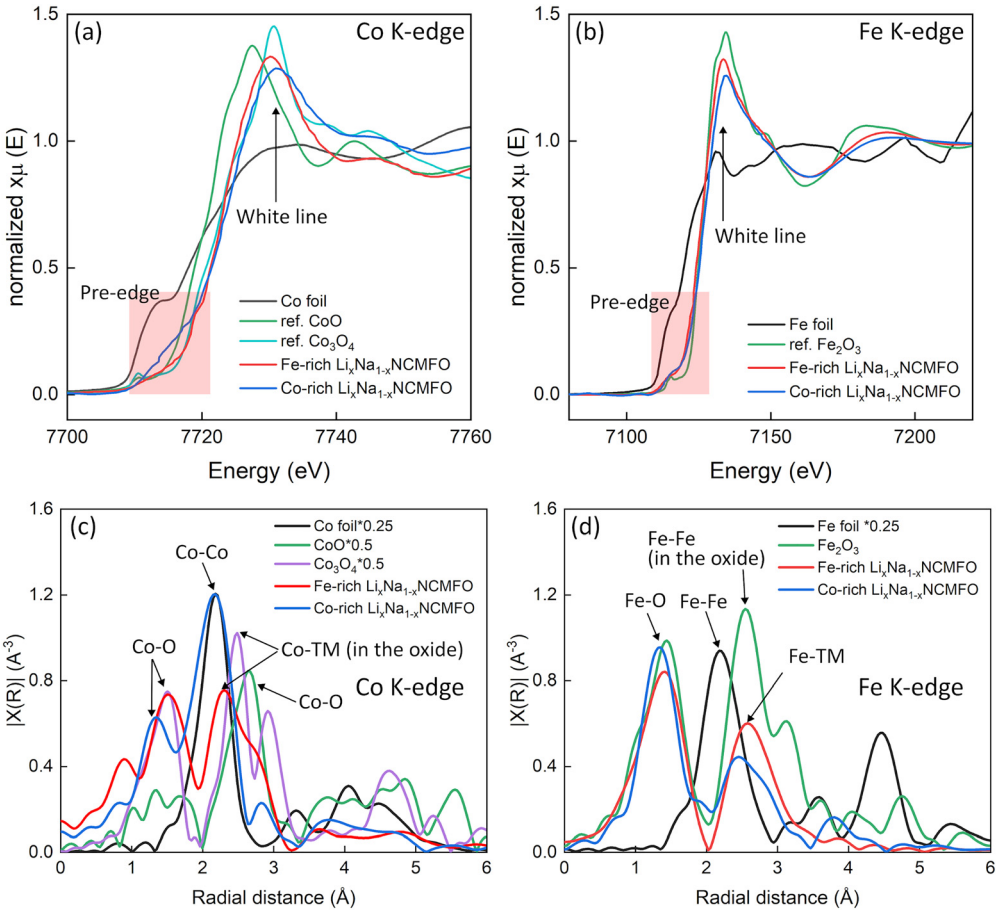

Fig. 2 XANES spectra of Co-rich and Fe-rich $Li_xNa_{1-x}(NiCoMnFe)O_2$ high entropy layered oxides at (a) Co K-edge and (b) Fe K-edge. Corresponding FT-EXAFS spectra at the (c) Co K-edge and (d) Fe K-edge. Spectra are not corrected for phase shift.

(XAS) on two representative samples: Co-rich and Fe-rich Li_xNa_{1-x}NCMFO. X-ray absorption near-edge structure (XANES) was used to assess the average oxidation state and electronic structure of each metal, while Fourier-transformed extended X-ray absorption fine structure (FT-EXAFS) provided information on the local geometric environment around the absorbing atoms. Fig. 2(a) and (b) present the Co and Fe K-edge spectra for the Fe-rich and Co-rich compositions. Ni and Mn K-edge spectra are shown in Fig. S1(a) and (b). In all four edges the samples display enhanced white-line intensities and a positive shift of the absorption edge relative to the corresponding metal foils, indicative of oxidized metal species. The XANES features are consistent with mixed valence behavior, broadly assignable to Ni^{2+}/Ni^{3+}, Co^{2+}/Co^{3+}, Mn^{2+}/Mn^{3+} and predominantly Fe^{3+} with small Fe^{2+}.

The corresponding FT-EXAFS analyses of the Fe-rich and Co-rich samples are shown in Fig. 2(c) and (d). In the Co K-edge spectrum, a strong Co–O first-shell peak appears at 1.47 Å, along with a weaker Co–M second-shell feature at 2.32 Å, which partially overlaps with Ni-related scattering. The positions and relative amplitudes of these peaks differ significantly from those of Co_3O_4 and CoO, reflecting the unique local bonding environment in the high-entropy oxide. A peak around 2.1 Å corresponds to Co–Co metallic bonding, consistent with Co foil references. This metallic Co feature is more pronounced in the Co-rich sample than in the Fe-rich analogue. The presence of a small fraction of metallic Co (possibly as nanoclusters undetectable by all methods) is also supported by a shoulder in the XANES pre-edge region (Fig. 2(a)). By contrast, the Fe-rich sample shows no detectable Fe–Fe metallic bonding, despite clear Fe–O first-shell and Fe–TM second-shell coordination. Thus, metallic contributions are evident only in the Co-rich sample and negligible in the Fe-rich one, demonstrating that enrichment in a particular transition metal does not necessarily induce partial reduction. Instead, the tendency toward reduction appears governed by each element's intrinsic redox potential and its local chemical environment.

Similar trends appear at the Ni and Fe K-edges (Fig. S1(c) and (d)). In all spectra, well-defined TM–O first-shell and TM–TM second-shell peaks are present, with amplitudes and positions that vary systematically with composition. Systematic peak shifts indicate composition-dependent changes in TM–O and TM–TM bond lengths. Overall, the FT-EXAFS data confirm octahedral TM–O coordination and pronounced TM–TM correlations consistent with an O3-type (α-$NaFeO_2$) layered lattice. These results reveal subtle, composition-dependent distortions

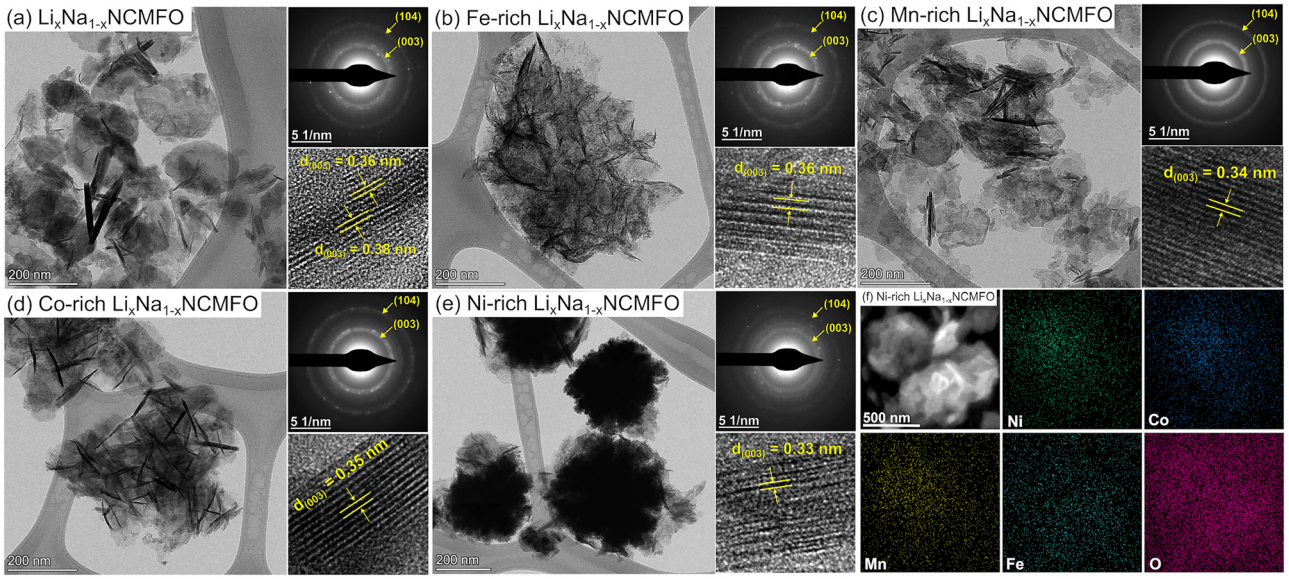

Fig. 3 (a)–(e) HRTEM, SAED and *d*-interplanar spacing of the synthesized samples and their formation mechanisms. (f) FESEM and EDS mapping of the Ni-rich $Li_xNa_{1-x}NiCoMnFeO_2$ sample.

in the first and second coordination shells, substantiate formation of the intended high-entropy layered oxide, and provide structural insight into the factors governing its electrochemical behavior.

The morphologies of the synthesized samples were examined using TEM, as illustrated in Fig. 3(a)–(e). The $Li_xNa_{1-x}NiCoMnFeO_2$ sample (Fig. 3(a)) exhibits ultrathin nanosheet structures comprising multiple stacked layers, with lateral dimensions on the order of several hundred nanometers, characteristic of O3-type layered oxides. Upon enrichment with Fe and Co, the nanosheets undergo a pronounced morphological transformation, forming aggregated, curved sheet assemblies with crumpled edges. While the overall arrangement may appear "flower-like," the observed dark lines could also correspond to overlapping plates viewed edge-on. These features may be attributable to increased lattice strain and interlayer interactions induced by the higher transition-metal content (Fig. 3(b) and (d)). In contrast, the Mn-rich sample retains a morphology analogous to the pristine $Li_xNa_{1-x}NiCoMnFeO_2$, consistent with the presence of a secondary layered $NaMnO_2$ phase, with only small aggregation. Ni-rich samples (Fig. 3(e)) diverge sharply, forming smooth, spherical aggregates rather than lamellar stacks, suggesting a reconfiguration of nucleation and growth kinetics in Ni-rich environments. This morphology aligns with established synthesis routes for Ni-dominant layered oxides, where Ni-rich environments promote the formation of dense, spherical secondary particles due to co-precipitation kinetics, as suggested in a previous study.[46] HRTEM imaging of all compositions reveals well-defined lattice fringes, from which $d_{(003)}$ spacings were measured and compared across all the samples. The pristine $Li_xNa_{1-x}NiCoMnFeO_2$ exhibits two spacings of 0.36 and 0.38 nm, with the slight variation likely reflecting local structural differences arising from Li/Na co-substitution in the alkali metal layer. The Fe-rich, Co-rich, Mn-rich, and Ni-rich variants yield spacings of 0.36, 0.35, 0.34, and 0.33 nm, respectively, with the relatively smaller value observed for the Ni-rich composition broadly consistent with the smaller ionic radius of Ni^{3+}/Ni^{4+} and the corresponding reduction in interslab distance along the *c*-axis. These measured spacings are in reasonable agreement with the XRD analysis. The SAED patterns (Fig. 3a–e, insets) display diffraction rings that can be indexed to the (003) and (104) reflections of the layered oxide phase, suggesting the retention of crystallographic order in the enriched samples and the absence of apparent spinel or rock-salt impurity phases. Additionally, EDS elemental mapping of the Ni-rich composition (Fig. 3(f)) indicates a relatively uniform spatial distribution of Ni, Co, Mn, Fe, and O across the spherical aggregates, which is generally consistent with the formation of a compositionally homogeneous high entropy material.

HER and OER performance of $Li_xNa_{1-x}NCMFO$

The electrochemical performance of the $Li_xNa_{1-x}NCMFO$ series toward both the HER and OER was systematically investigated in 1 M KOH using a conventional three-electrode configuration. The working electrode was prepared by drop-casting the catalyst ink onto a 3 mm glassy carbon electrode (GCE) with a catalyst loading of 1 mg cm^{-2}. A Hg/HgO electrode and a graphite rod were employed as the reference and counter electrodes, respectively (see the SI for details). Prior to LSV, the catalyst electrodes were conditioned by CV activation scans to remove surface contaminants and establish a stable electrode–electrolyte interface. Thereafter, LSV was carried out at a scan rate of 5 mV s^{-1}, with full iR compensation applied throughout. For HER testing, potentials were swept from 0 V to −0.8 V vs RHE, and the overpotential required to achieve a current density of 10 mA cm^{-2} (η_{10}) was recorded as the primary metric of catalytic activity: the lower the η_{10}, the more kinetically efficient the electrode. Fig. 4(a) clearly demonstrates

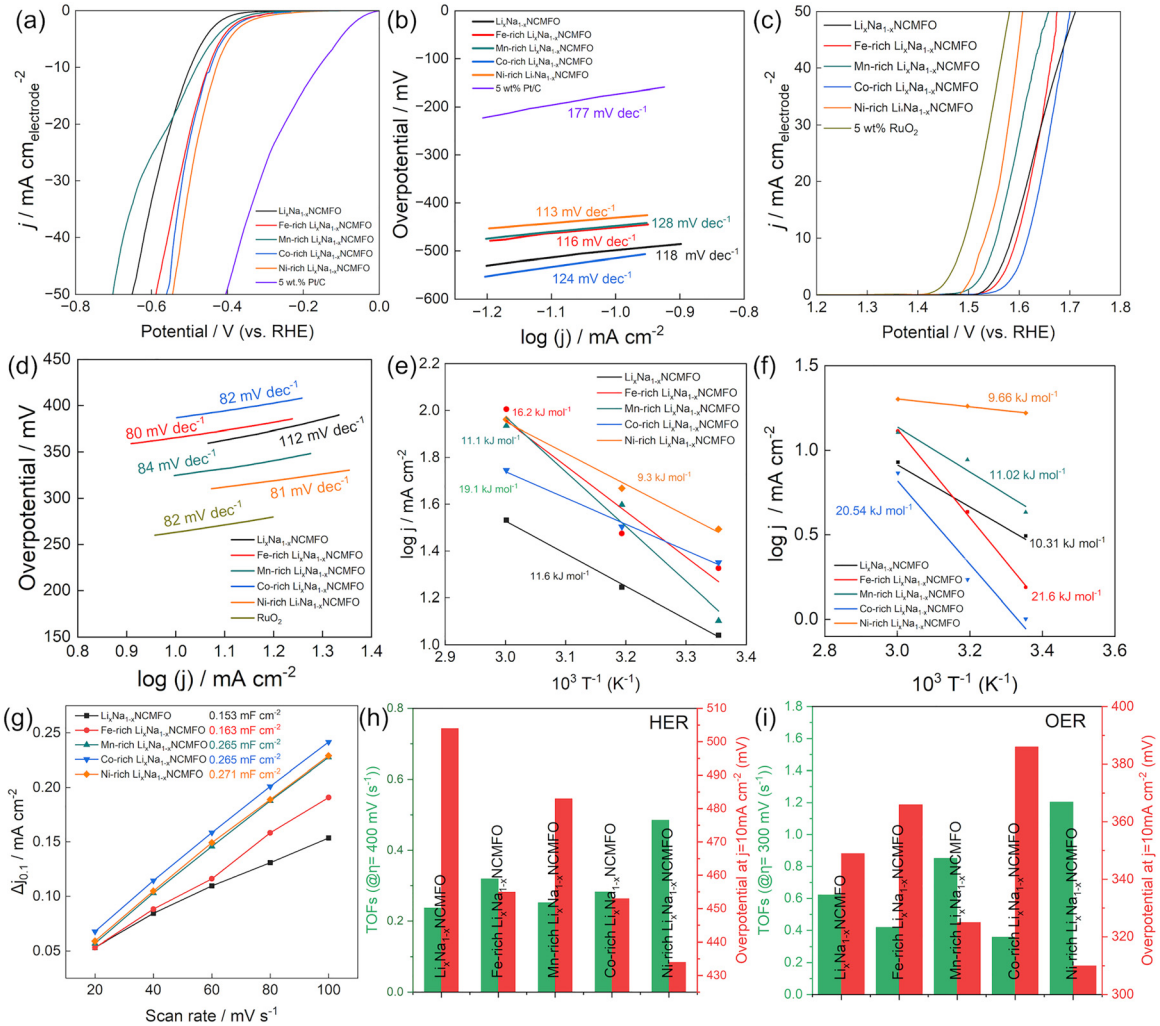

Fig. 4 (a) HER LSV curves at 5 mV s^{-1}, (b) HER Tafel slope, (c) OER LSV curves at 5 mV s^{-1}, and (d) OER Tafel slope. Arrhenius plots for the (e) HER and (f) OER. (g) C_{dl} estimation for ECSA calculation taken at 1 V vs RHE. Calculated TOF and η at 10 mA cm^{-2} for the (h) HER and (i) OER.

that the Li$_x$Na$_{1-x}$NCMFO sample exhibits the poorest HER activity, manifesting an η_{10} of 504 mV. Strategic addition of transition metals progressively lowers this overpotential It was observed that the η_{10} reduced to 483 mV, 455 mV, 453 mV, and 434 mV when the samples were enriched with Mn, Fe, Co, and Ni, respectively. Although none of these samples approaches the benchmark performance of commercial 5 wt% Pt/C ($\eta_{10} \approx 160$ mV), triplicate measurements confirm that the trends are both reproducible and statistically significant. The Ni-rich Li$_x$Na$_{1-x}$NCMFO electrode not only displayed the lowest η_{10} but also achieved the highest current densities throughout the polarization range, indicative of enhanced active-site density and accelerated Volmer–Heyrovsky reaction kinetics. This interpretation is corroborated by Tafel analysis in Fig. 4(b), in which the Ni-rich Li$_x$Na$_{1-x}$NCMFO electrode exhibits a slope of 113 mV dec^{-1}, smaller than those of the Fe-, Mn-, and Co-rich samples (116–128 mV dec^{-1}) and on par with 5 wt% Pt/C (117 mV dec^{-1}), which reflects more favorable hydrogen adsorption and desorption dynamics.

Under identical experimental conditions, OER polarization curves were recorded from 1.2 to 1.8 V *versus* RHE. Once again, the bare Li$_x$Na$_{1-x}$NCMFO sample proved the least active, requiring an η_{10} of 349 mV and exhibiting a Tafel slope of 112 mV dec^{-1}. Enriched electrodes displayed smaller η_{10} in the order Co-rich (386 mV), Fe-rich (366 mV), Mn-rich (325 mV), and Ni-rich (310 mV), with the Ni-rich Li$_x$Na$_{1-x}$NCMFO sample also delivering the lowest OER Tafel slope of 81 mV dec^{-1}. For comparison, commercial RuO_2 was tested under the same protocol, achieving an η_{10} of 264 mV and a Tafel slope of 82 mV dec^{-1}, thereby affirming that the Ni-rich Li$_x$Na$_{1-x}$-NCMFO catalyst offers bifunctional activity towards the HER and OER approaching state-of-the-art noble-metal benchmarks. Taken together, these results show that the Ni-rich Li$_x$-Na$_{1-x}$NCMFO material outperforms all other compositions, delivering activity on a level comparable to that of similar catalysts produced from battery-waste precursors (see Table 1 for details).

To elucidate the temperature dependence of catalytic kinetics, LSV experiments for both the HER and OER were conducted at 25, 40, and 60 °C. As illustrated in Fig. S2 and S3, elevating the electrolyte temperature markedly increases

Table 1 Comparison of the HER and OER activities of spent-battery derived electrocatalysts operated at a current density of 10 mA cm^{-2} at room temperature (25 °C)

No.	Catalyst	Electrolyte	η at 10 mA cm^{-2} (mV)		Tafel (mV dec^{-1})		Ref.
			HER	OER	HER	OER	
1	NiCoMnFe–LDH/C	1 M KOH	—	329	—	66	23
2	α-$Co(OH)_2$	1 M KOH	—	131	—	80.2	24
3	NiCoMnB	1 M KOH	—	263	—	57.9	47
4	$Ni_{0.5}Mn_{0.3}Co_{0.2}(OH)_2$	1 M KOH	—	280	—	67.9	25
5	Ni–$LiFePO_4$	1 M KOH	—	285	—	45	48
6	$LiCoO_{2-x}Cl_x$	1 M KOH	—	360	—	53.6	49
7	$LiNi_{0.94}Co_{0.05}Mn_{0.01}O_2$	1 M KOH	—	270	—	121	50
8	$Li_{1+x}(NiCoMn)O_2$	1 M KOH	58	222	72	72.9	51
9	CoN–Gr	1 M KOH	128.9	280	67.3	68.8	26
10	Ni-rich Li_xNa_{1-x}NCMFO	1 M KOH	434	310	113	81	This work

kinetic current densities at potentials below 1.6 V vs RHE for all five compositions. The plots of Arrhenius analyses depicted in Fig. 4(e and f), performed at a fixed potential of 1.55 V, where mass-transport limitations are negligible, reveal a linear relationship between the logarithm of the current density ($\log j$) and the reciprocal temperature ($1/T$), consistent with the classical Arrhenius expression $j_{(1.55\ V)} = Ze^{\left(\frac{-E_a}{RT}\right)}$. From these plots, the Ni-rich electrode exhibited the lowest activation energy (E_a) for both the HER and OER. This confirms that nickel substitution lowers the energetic barriers for electron transfer and intermediate adsorption, thereby improving overall catalytic activity.

The electrochemically active surface area (ECSA) was quantified *via* double-layer capacitance (C_{dl}) measurements obtained from CV scans in a non-faradaic potential window (0.8–1.4 V *vs.* RHE) at varying scan rates (see Fig. S4). C_{dl} was extracted from the slope of the current-density change (Δj) at 1.1 V *vs.* RHE plotted against scan rate (Fig. 4(g)). ECSA was then calculated as C_{dl} divided by the specific capacitance (C_s = 0.04 mF cm^{-2}, equivalent to 40 μF cm^{-2}) of a 3 mm-diameter glassy-carbon electrode in 1 M KOH. The Ni-rich sample exhibited the highest ECSA (0.39 cm^2), followed by Fe-rich (0.27 cm^2), Mn-rich (0.25 cm^2), bare sample (0.13 cm^2) and Co-rich (0.11 cm^2). This suggests that an enriched sample with Ni created a high density of active sites for both the HER and OER, promoting fast ion and electron transport in the electrolyte and driving the observed enhancement in catalytic activity. The calculated TOF at η_{HER} = 400 mV and η_{OER} = 300 mV (Fig. 4(g)) indicates comparable intrinsic activity across all compositions. However, the Ni-rich Li_xNa_{1-x}NCMFO electrode achieved the highest turnover frequencies of 0.48 s^{-1} for the HER and 1.20 s^{-1} for the OER, which is approximately 1.5 to 2 times greater than those for the other samples. TOF measures the number of reactant molecules converted by each active site per second, reflecting intrinsic catalytic efficiency. A higher TOF means that each catalytic site on the Ni-rich sample operates more rapidly, independent of surface area or catalyst loading.

Furthermore, intrinsic activity was evaluated by normalizing the current density to the ECSA (Fig. S5). Upon ECSA normalization, the Co-rich sample displayed the highest HER activity, while OER activities were comparable across all compositions. These observations suggest that while Co sites may exhibit superior intrinsic HER kinetics, the overall performance at the device level is governed by the total number of accessible active sites rather than solely by per-site activity. Consequently, for practical electrochemical devices, geometric current densities, which reflect the combined contributions of ECSA and intrinsic activity, are more relevant metrics than ECSA-normalized values, as they directly correlate with device-level performance.

Following individual half-reaction HER and OER tests, we evaluated the Ni-rich Li_xNa_{1-x}NCMFO sample in a full water-splitting cell. Due to its superior half-cell activity, the Ni-rich sample was employed as both the cathode and anode, with 5 wt% Pt/C (cathode) and RuO_2 (anode) serving as benchmarks. 1 mg cm^{-2} of catalyst loadings were deposited on carbon paper on each electrode. As shown in Fig. 5(a), the all–Ni-rich device required overpotentials (η) of 580 mV for the HER at 50 mA cm^{-2}, and, for the OER, η_{50} = 425 mV and η_{100} = 479 mV. These values exceed those measured in the three-electrode configuration, an expected outcome given the superior kinetics of the Pt counter-electrode used previously. In contrast, the 5 wt% Pt/C‖RuO_2 cell achieved η_{50} and η_{100} of 133 mV and 218 mV for the HER, and 329 mV and 403 mV for the OER. The Tafel slope (Fig. 5(b)) of the benchmark cell was lower than that of the Ni-rich system, confirming faster reaction kinetics. In an H-cell stability test at 1.7 V *vs.* RHE (Fig. 5(c)), both cells exhibited gradual current decay, likely due to hydrogen and oxygen gas bubble accumulation at the catalyst surface, which impeded mass transport. The measured hydrogen-production rates were 0.0192 mmol min^{-1} $mg_{cat.}{}^{-1}$ for Pt/C‖RuO_2 and 0.0147 mmol min^{-1} $mg_{cat.}{}^{-1}$ for all the Ni-rich electrodes (Fig. 5(d)), with a faradaic efficiency of up to 64%. To assess the performance under practical operating conditions, the Ni-rich Li_xNa_{1-x}NCMFO was also evaluated in a commercial flow-electrolyzer cell. Cyclic voltammograms recorded at 20 and 50 mV s^{-1} (Fig. 5(e)) revealed a marked rise in current density started at 1.9–2.0 V, beyond which the current density declined and exhibited increased noise. This behavior is attributed to gas-bubble accumulation on the electrode surface, which hinders active-site accessibility. Increasing the flow rates of both the catholyte and anolyte can accelerate bubble desorption and removal, thereby maintaining clean catalyst surfaces.

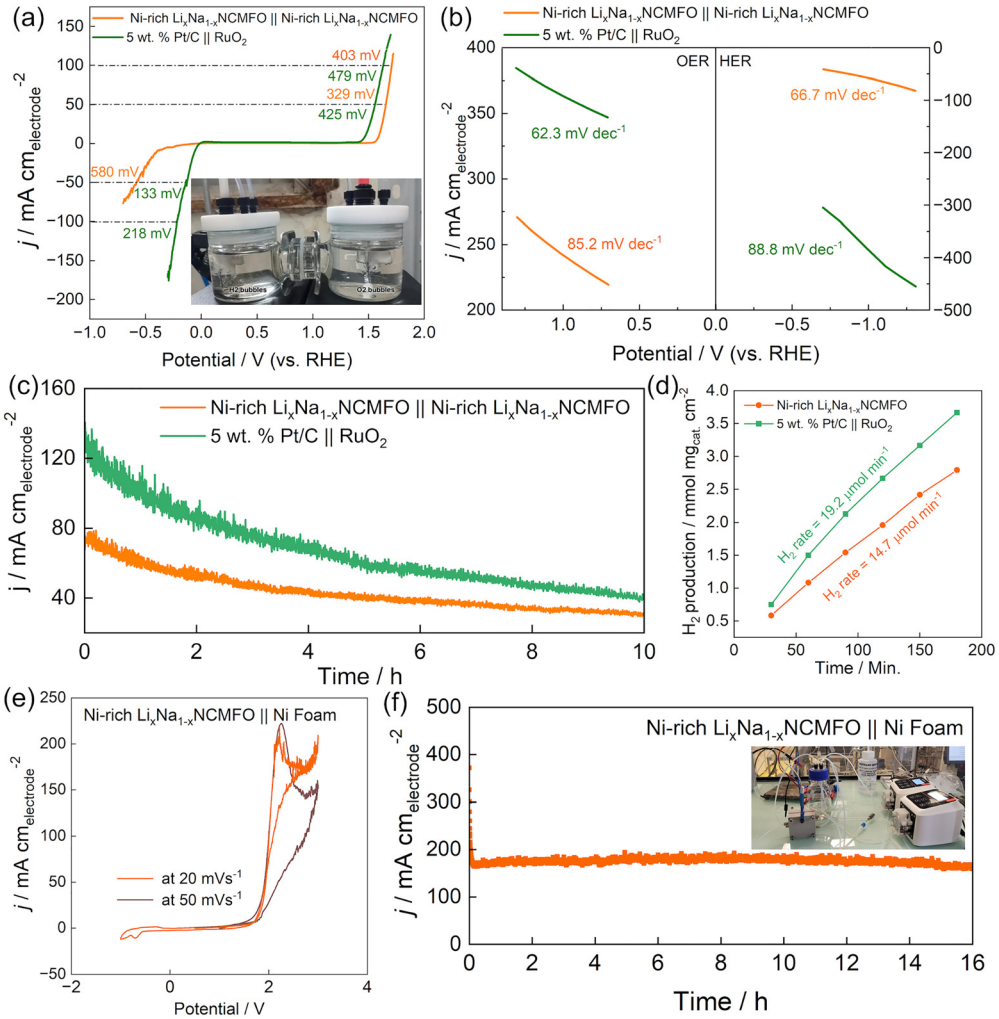

Fig. 5 (a) LSV polarization curves comparing Ni-rich $Li_xNa_{1-x}NCMFO||$Ni-rich $Li_xNa_{1-x}NCMFO$ and 5 wt% Pt/C||RuO_2. (b) Tafel slopes derived from overall water-splitting polarization data. (c) Chronoamperometric stability test at 1.7 V *vs.* RHE. (d) Quantified H_2 evolution during water splitting. (e) Cyclic voltammograms of Ni-rich $Li_xNa_{1-x}NCMFO||$Ni foam in a flow electrolyzer cell, recorded at 20 and 50 mV s^{-1}. (f) Long-term chronoamperometry at 2.0 V *vs.* RHE for the Ni-rich $Li_xNa_{1-x}NCMFO||$Ni foam electrode.

Under these flow conditions, the electrocatalyst exhibited enhanced stability, with only a slight decline in current density over 16 h of operation (Fig. 5(f)), reflecting the optimized mass-transport dynamics in the flow electrolyzer.

Electrochemical HMF oxidation

Building on the promising performance of the catalyst for overall water splitting, we further investigated its applicability for HMF oxidation. This approach enables the simultaneous production of hydrogen at the cathode and value-added chemical conversion of HMF at the anode. Notably, recent life cycle assessments suggest that HMF/H_2O co-electrolysis offers a lower environmental impact compared to separate electrolytic processes for HMF and water.[52,53] Fig. 6(a) and (b) show the CV and LSV profiles comparing HMF oxidation (10 mM HMF in 1 M KOH) and water oxidation (1 M KOH, HMF-free) using both $Li_xNa_{1-x}NCMFO$ and Ni-rich $Li_xNa_{1-x}NCMFO$ electrodes. In the absence of HMF, both samples exhibit a pair of redox peaks centered at 1.33 V and 1.40 V *vs.* RHE, characteristic of the Ni^{2+}/Ni^{3+} redox couple. These peaks are typically observed in alkaline media within the range of 1.35–1.55 V and are associated with the generation of catalytically active high-valent nickel species.[22] Upon addition of HMF, the redox features become broader and shift toward lower potentials, suggesting that Ni^{3+} species participate directly in the oxidation of HMF, being reduced back to Ni^{2+} during the process. This behavior supports a mechanism in which HMF oxidation proceeds *via* initial activation of its functional groups through hydration, facilitated by OH^- ions.[18] Subsequent deprotonation of C–H or O–H bonds at the catalyst surface drives the oxidation process. The Ni-rich electrode shows an onset potential of 1.55 V *vs.* RHE for water oxidation and achieves 20 mA cm^{-2} at 1.58 V *vs.* RHE. With HMF present, the onset potential decreases to 1.50 V *vs.* RHE, and 20 mA cm^{-2} is reached at 1.53 V *vs.* RHE, highlighting that HMF oxidation is more favorable than water oxidation at lower applied potentials.

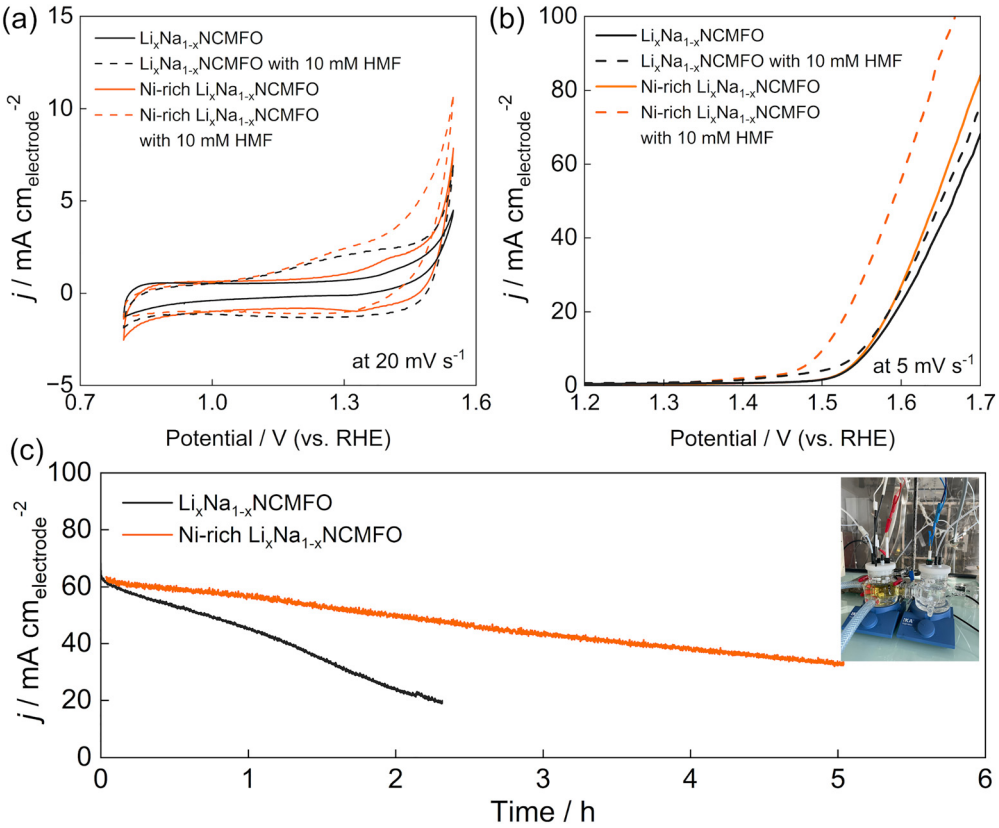

Fig. 6 (a) CV and (b) LSV polarization curves of comparing HMF oxidation (10 mM HMF in 1 M KOH) and water oxidation (1 M KOH, HMF-free) using both Li_xNa_{1-x}NCMFO and Ni-rich Li_xNa_{1-x}NCMFO electrodes (c) Chronoamperometry of the samples in 10 mM HMF with 1 M KOH electrolyte.

In comparison, the Li_xNa_{1-x}NCMFO exhibits lower activity for both HMF and water oxidation, reinforcing the enhanced catalytic behavior of the Ni-rich Li_xNa_{1-x}NCMFO for selective and efficient HMF electrooxidation. To assess conversion performance, chronoamperometric oxidation was conducted at 1.6 V *vs.* RHE in the presence of 10 mM HMF. As shown in Fig. 6(c), the Ni-rich catalyst maintained more stable current over time, while the Li_xNa_{1-x}NCMFO sample showed a rapid decline after approximately 2.5 hours of continuous operation, indicating lower durability. Faradaic efficiency (FE) is summarized in Fig. 6(d). The Ni-rich Li_xNa_{1-x}NCMFO achieved an FE of 18.7% toward FDCA and 0.94% toward FCA, whereas the Li_xNa_{1-x}NCMFO sample delivered only 10.6% FE for FDCA with no detectable FCA formation. Similar to water electrolysis, the Ni enrichment may play an important role in the electrocatalytic HMF conversion and product selectivity. While these FE values are lower than those reported for recent state-of-the-art Ni-based electrocatalysts (Table S3), it is important to emphasize that our catalyst is derived from spent battery cathodes, which to our knowledge has not been previously reported for this reaction. This study therefore represents a proof-of-concept for transforming battery waste into functional electrocatalysts. Beyond activity metrics alone, our approach offers important advantages in terms of sustainability, resource recovery, and waste valorization, providing a low-cost and environmentally responsible pathway for catalyst production.

Electrocatalytic enhancement mechanism

Traditionally, the superior electrochemical in the Ni-rich sample may arise from: (i) enhanced active-site density, as Ni incorporation can expose more catalytically favorable sites; (ii) improved electronic conductivity, which accelerates charge transfer; and (iii) optimized binding energies for reaction intermediates, facilitating better adsorption–desorption kinetics for both H_{ads} in the HER and OH/OOH species in the OER.[54] In our case, we propose that the enhanced electrocatalytic activity of the Ni-rich Li_xNa_{1-x}NCMFO may arise from a synergistic combination of (i) structural, (ii) electronic, and (iii) surface effects. (i) Structural characterization reveals that Ni incorporation shortens TM–O bond lengths and strengthens TM–O interactions, thereby stabilizing reaction intermediates and facilitating charge transfer, as previously demonstrated in urea electrooxidation.[55] The high-entropy configuration further introduces local lattice distortions and synergistic interactions among Ni, Co, Mn, and Fe, leading to optimized electronic states and reduced activation barriers, which tune the adsorption energies of key intermediates such as H* in the HER and *O/*OOH in the OER.[56] (ii) XPS analysis (Fig. S6 and Table S4) shows that the Ni-rich composition contains a higher fraction of Ni^{3+} species (more active than Ni^{2+}) and oxygen vacancies compared with other samples; both features are widely reported to enhance catalytic activity by increasing the density of electrochemically active sites and promoting more surface redox reactions.[57–59] (iii) Electrochemical

measurements are in agreement with these findings, as Ni enrichment substantially increases both the electrochemically active surface area and turnover frequency, indicating not only a greater density of accessible sites but also higher intrinsic activity per site. Notably, despite its moderate BET surface area (123.7 $m^2\ g^{-1}$) (Fig. S7 and Table S5), the Ni-rich catalyst delivers superior performance, highlighting that electrochemically active-site density rather than physical surface area governs catalytic behavior. Beyond structural and electronic contributions, multi-functionality further enhances catalytic efficiency through the coupling of water splitting with selective HMF oxidation. In this process, high-valent Ni^{3+} species serve as active centers, enabling HMF electrooxidation at lower potentials than the OER and thereby reducing the overall energy input while co-producing hydrogen and value-added FDCA. The schematic illustration of the enhanced electrochemical co-production of hydrogen and FDCA on the Ni-rich Li_xNa_{1-x}NCMFO high entropy layered oxide catalyst is shown in Fig. 7.

Post-reaction characterization analyses (XRD, Fig. S8; XPS, Fig. S9; and TEM, Fig. S10) reveal that the synthesized catalysts undergo subtle structural evolution during the electrocatalytic process. While the overall crystal structure is largely preserved (Fig. S8) and their morphology is retained (Fig. S10), the XPS analysis (Fig. S9) discloses meaningful changes in the electronic structures of the constituent transition metals. Specifically, in the Ni 2p core-level spectra (Fig. S9a), the relative intensity of the satellite peaks and the binding energy positions of the Ni $2p_{3/2}$ and Ni $2p_{1/2}$ components shift after the electrocatalytic reaction, suggesting a partial oxidation-state transition of Ni ions. Similarly, the Co 2p spectra (Fig. S9b) reveal alterations in the Co^{2+}/Co^{3+} ratio, as evidenced by the redistributed satellite peak intensities, indicative of Co oxidation-state fluctuations driven by the electrochemical environment. The Fe 2p and Mn 2p spectra (Fig. S9c and d) also exhibit changes in their spin–orbit splitting components and corresponding satellite features, pointing to partial redox transformations of Fe and Mn centers under operating conditions. We, based on this fact, suggest that the transition metal sites may act as active redox mediators during catalysis, consistent with the proposed reaction mechanism. Furthermore, the O 1s spectra (Fig. S9e) show a notable redistribution among the lattice oxygen, metal–oxygen bond, and surface-adsorbed oxygen species between the fresh and post-reaction samples, implying dynamic oxygen vacancy formation and surface hydroxylation during the electrocatalytic process. Additionally, the Na 1s spectra (Fig. S9f) indicate a slight reduction in the Na signal intensity after the reaction, suggesting partial Na leaching or surface redistribution.

Life cycle assessment (LCA)

A cradle-to-gate LCA was performed to evaluate the environmental implications of the end-to-end process, from spent cathode recycling to co-electrocatalytic production of hydrogen and HMF oxidation products, using the system boundary illustrated in Fig. S11. Two scenarios were compared: (i) hydrogen production only and (ii) hydrogen production with FDCA co-generation *via* HMF electrooxidation. As summarized in Table S6, the allocation-based scenario that treats FDCA as a co-product (ii) yields systematically lower impacts across the assessed categories than the hydrogen-only scenario (i), reflecting the benefit of environmental impacts sharing between hydrogen and FDCA. Contribution analysis of scenario (i) and (ii) as shown in Fig. 8(a) and (b), respectively, identified the electrocatalytic step, driven primarily by electricity consumption during electrolysis, as the dominant hotspot in both scenarios. Because this assessment is based on laboratory-scale operation, several scale-dependent assumptions merit consideration. Laboratory measurements of cell voltage, current density, faradaic efficiency, and material inventories were normalized to the functional unit and extrapolated to continuous operation; at commercial scale, these parameters are expected to evolve due to improved cell design, higher operating current densities, longer electrode lifetimes, and process integration. Given the dominance of electricity in the impact profile, improvements in energy efficiency (*e.g.*, reduced overpotentials or higher selectivity) would proportionally lower cradle-to-gate impacts, whereas additional energy demand associated with

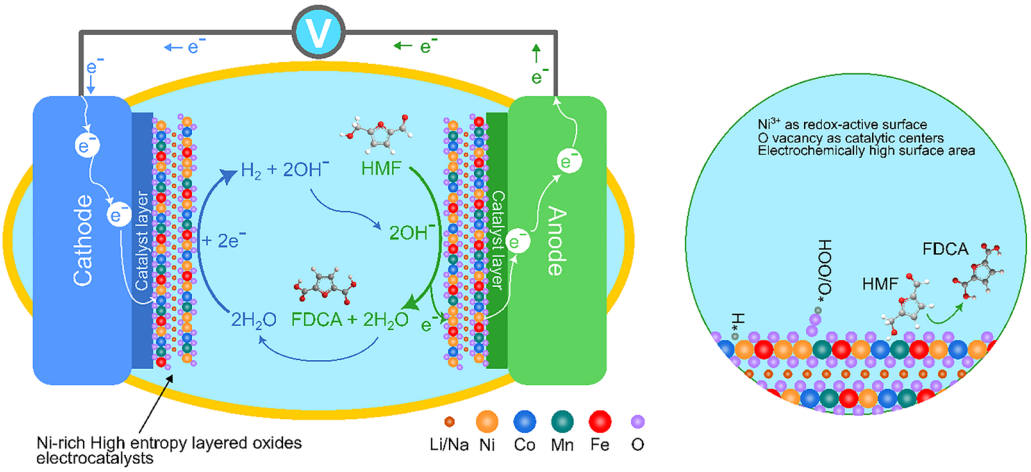

Fig. 7 A schematic illustration of the enhanced electrochemical co-production of hydrogen and FDCA on the Ni-rich Li_xNa_{1-x}NCMFO high entropy layered oxide catalyst.

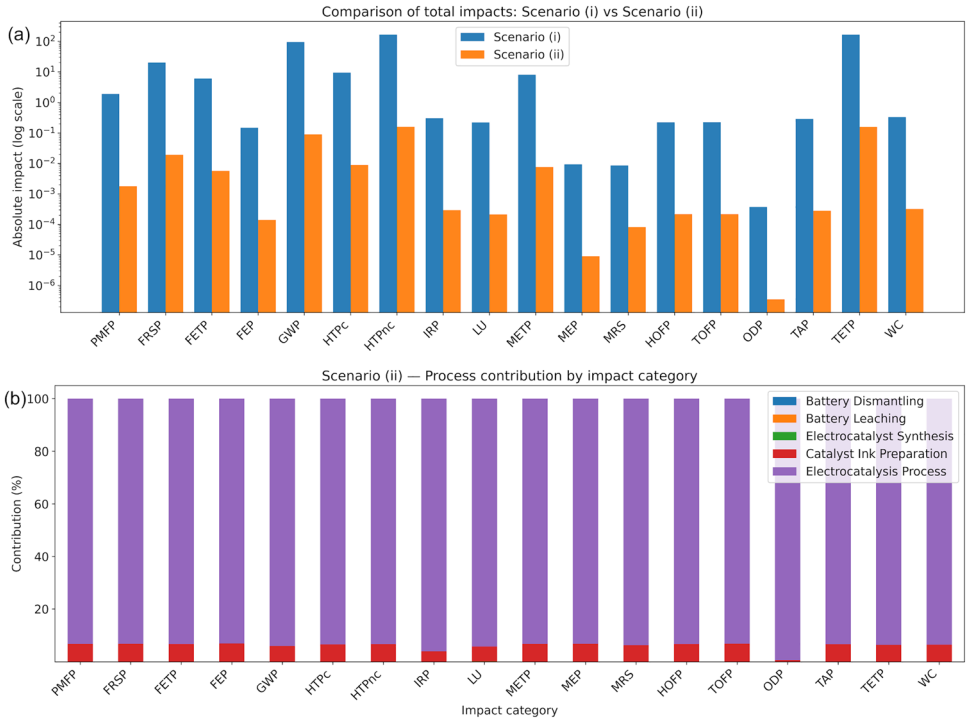

Fig. 8 (a) Life cycle impact assessment (LCIA) results for hydrogen production only (scenario (i)) and hydrogen production with FDCA co-generation *via* HMF electrooxidation (scenario (ii)). (b) Contribution analysis of the scenario (ii) by impact category.

downstream product separation and purification could partially offset these gains. Similarly, extending electrode and catalyst lifetimes at scale would reduce the per-unit contribution of material production and recycling, while shorter-than-expected lifetimes would increase impacts. Furthermore, the sensitivity analysis (Fig. S12 and Table S7) clearly highlights that the electricity source is the principal determinant of the cradle-to-gate environmental performance for hydrogen production coupled with FDCA co-generation. Decarbonizing the power supply markedly improves performance: hydropower delivers the largest reductions (most ReCiPe categories $>90\%$; GWP $\approx 80\%$ down from 9.04×10^{-2} to 1.81×10^{-2} kg CO_2-eq) but raises water use by $>465\%$, while solar PV achieves a similar GWP cut ($\sim 79.9\%$) yet shifts burdens (MRS +13.3%, TETP +30.9%, IRP +72% *versus* hydropower −43%) with ODP essentially unchanged. These results show that while absolute impact magnitudes may shift upon scale-up, the relative trends and dominant drivers remain robust, showing that product multifunctionality and, critically, the electricity source are the principal levers for lowering the cradle-to-gate footprint, and that regional selection of generation technologies is needed to avoid burden-shifting and balance trade-offs.

Conclusions

We have developed a low-temperature, sustainable route to synthesize high-entropy layered oxides, $Li_xNa_{1-x}(NiCoMnFe)O_2$, directly from spent lithium-ion battery cathodes. A Ni-rich composition shows superior trifunctional activity, achieving η_{10} of 434 mV for the HER and 310 mV for the OER with Tafel slopes near noble-metal benchmarks, and enabling co-electrolysis of water and HMF to produce hydrogen (FE $\sim$ 64%) and FDCA (FE $\sim$ 18%) with good durability for more than 17 h in a flow-electrolyzer. Life-cycle assessment indicates that FDCA co-production reduces the environmental burden relative to hydrogen alone, and renewable electricity further cuts impacts by $\sim$80%, albeit with trade-offs in water use (hydropower) or resource intensity (solar PV). These results demonstrate that LIB waste can be directly valorized into multifunctional electrocatalysts, coupling circularity with sustainable hydrogen and chemical production.

Author contributions

UMN: investigation, visualization, writing – original draft. ADF: methodology, software. SR and AH: conceptualization, methodology, resources. NLWS and MK: writing – review & editing, HB: methodology, software, writing – original draft. IBA, AZ and AD: investigation, resources, validation. MP: resources, supervision, writing – review & editing. LWH: supervision, writing – review & editing, AH: conceptualization, methodology, validation, formal analysis, writing – review & editing, funding acquisition.

Conflicts of interest

The authors promise that there are no conflicts of interest to declare.

Data availability

The data supporting this article have been included as part of the supplementary information (SI). Supplementary information: Methods: Full experimental protocols for battery leaching, catalyst synthesis, electrochemical measurements (HER, OER, overall water splitting, HMF oxidation), and Faradaic efficiency calculations. Tables: ICP-OES leaching efficiency (S1), elemental composition and mixing entropy (S2), XPS deconvolution (S4), BET surface area and pore data (S5), HMF oxidation benchmarking against literature (S3), and LCA impact categories with sensitivity analysis (S6, S7). Figures: XANES/FT-EXAFS spectra (S1), temperature-dependent HER/OER LSV curves (S2, S3), CV at variable scan rates (S4), ECSA-normalized LSV (S5), full XPS core-level spectra (S6), N2 adsorption isotherms and pore size distributions (S7), post-catalysis XRD (S8), XPS (S9), and HRTEM/SAED (S10), plus the LCA system boundary diagram (S11) and sensitivity analysis chart (S12). LCA: Cradle-to-gate environmental impact assessment for hydrogen-only and H2/FDCA co-production scenarios, with sensitivity analysis across grid mix, hydropower, and solar PV electricity sources. See DOI: https://doi.org/10.1039/d6mh00184j.

Acknowledgements

This research was partially funded by the STIC U.S.–ASEAN Research and Publishing Seed Grant. A.H. gratefully acknowledges *Science et Impact* (French Embassy) for supporting a mobility grant. Additional support was provided by the LPDP Grant and BRIN through the RIIM International Collaboration Southeast Asia–European Joint Funding Scheme (grant numbers B-18/II.7.5/FR.06/1/2025 and B-5/III-10/FR.06.00/1/2025). MK would like to acknowledge the financial support of the Directorate of Research Funding and Ecosystem, Universitas Indonesia, through Hibah PUTI Top Tier 2025 (Contract No. PKS-169/UN2.R3/HKP.05.00/2025). We thank Itzcóatl Rafael Garduño Ibarra and Zhi Gang for the HPLC measurements. The authors also thank the characterization facilities of the National Research and Innovation Agency's E-Layanan Sains. They further acknowledge the use of Grammarly for assistance with language editing. The authors retain full responsibility for the content and analysis presented in this paper.

References

1 G. G. Njema, R. B. O. Ouma and J. K. Kibet, *J. Renewable Energy*, 2024, **2024**, 1–35.
2 G. Zubi, R. Dufo-López, M. Carvalho and G. Pasaoglu, *Renewable Sustainable Energy Rev.*, 2018, **89**, 292–308.
3 Y. Liang, C. Z. Zhao, H. Yuan, Y. Chen, W. Zhang, J. Q. Huang, D. Yu, Y. Liu, M. M. Titirici, Y. L. Chueh, H. Yu and Q. Zhang, *InfoMat*, 2019, **1**, 6–32.
4 K. Nováková, A. Pražanová, D. I. Stroe and V. Knap, *Energies*, 2023, **16**(5), 2345.
5 V. M. Leal, J. S. Ribeiro, E. L. D. Coelho and M. B. J. G. Freitas, *J. Energy Chem.*, 2023, **79**, 118–134.
6 H. Bae and Y. Kim, *Mater. Adv.*, 2021, **2**, 3234–3250.
7 B. K. Biswal, B. Zhang, P. Thi Minh Tran, J. Zhang and R. Balasubramanian, *Chem. Soc. Rev.*, 2024, **53**, 5552–5592.
8 J. J. Roy, D. M. Phuong, V. Verma, R. Chaudhary, M. Carboni, D. Meyer, B. Cao and M. Srinivasan, *Carbon Energy*, 2024, **6**(6), e492.
9 F. Te Tsai, Y. T. Deng, C. W. Pao, J. L. Chen, J. F. Lee, K. T. Lai and W. F. Liaw, *J. Mater. Chem. A*, 2020, **8**, 9939–9950.
10 A. Wu, Y. Xie, H. Ma, C. Tian, Y. Gu, H. Yan, X. Zhang, G. Yang and H. Fu, *Nano Energy*, 2018, **44**, 353–363.
11 S. Zhang, X. Cao, B. Wang, J. Wei, L. Zhou, J. Han and J. Yun, *Int. J. Hydrogen Energy*, 2025, **109**, 684–693.
12 H. Osgood, S. V. Devaguptapu, H. Xu, J. Cho and G. Wu, *Nano Today*, 2016, **11**, 601–625.
13 J. Lei, H. Zhang, J. Yang, J. Ran, J. Ning, H. Wang and Y. Hu, *J. Energy Chem.*, 2025, **100**, 792–814.
14 L. Guo, X. Zhang, L. Gan, L. Pan, C. Shi, Z. Huang, X. Zhang and J. Zou, *Adv. Sci.*, 2023, **10**(4), 2205540.
15 M. Zhang, Z. Zheng, X. Zhang, Z. Jiang, X. Yong, K. Li, X. Tu and K. Yan, *JACS Au*, 2025, **5**, 937–947.
16 Y. Yang and T. Mu, *Green Chem.*, 2021, **23**, 4228–4254.
17 M. T. Bender and K. Choi, *ChemSusChem*, 2022, **15**(13), e202200675.
18 L. Gouda, L. Sévery, T. Moehl, E. Mas-Marzá, P. Adams, F. Fabregat-Santiago and S. D. Tilley, *Green Chem.*, 2021, **23**, 8061–8068.
19 W.-J. Liu, L. Dang, Z. Xu, H.-Q. Yu, S. Jin and G. W. Huber, *ACS Catal.*, 2018, **8**, 5533–5541.
20 L. Wang, Y. Yan, R. Li, X. Han, J. Li, T. Ran, J. Li, B. Xiong, X. Song, Z. Yin, H. Wang, Q. Zhu, B. Cheng and Z. Yin, *Chinese Chem. Lett.*, 2024, **35**, 110011.
21 J. Zhang, Y. Yang, G. Ding, Z. Wang, P. Wang, C. Li and G. Liao, *Chem. Eng. J.*, 2025, **505**, 159165.
22 I. R. Garduño-Ibarra, Z. Yan, S. A. Ebrahim, E. Baranova, J. González-Cobos, M. Prévot and P. Vernoux, *ChemElectroChem*, 2025, **12**(13), e202500067.
23 A. Hermawan, N. S. R. Kinasih, R. Radiana, A. Nursyahid, S. Rahayu, D. A. Saputra, V. Puspasari, N. L. W. Septiani, A. Hardiansyah, M. D. Gumelar, E. L. Dewi, M. Aziz and S. Yin, *Int. J. Hydrogen Energy*, 2024, **89**, 254–263.
24 A. Kotkar, S. Dash, P. Bhanja, S. Sahu, A. Verma, A. Mukherjee, M. Mohapatra and S. Basu, *Electrochim. Acta*, 2023, **442**, 141842.
25 Y. Yang, H. Yang, H. Cao, Z. Wang, C. Liu, Y. Sun, H. Zhao, Y. Zhang and Z. Sun, *J. Cleaner Prod.*, 2019, **236**, 117576.
26 T. Liu, S. Cai, G. Zhao, Z. Gao, S. Liu, H. Li, L. Chen, M. Li, X. Yang and H. Guo, *J. Energy Chem.*, 2021, **62**, 440–450.
27 S. Bolar, Y. Ito and T. Fujita, *Chem. Sci.*, 2024, **15**, 8664–8722.
28 X. Yang, R. Guo, R. Cai, Y. Ouyang, P. Yang and J. Xiao, *Int. J. Hydrogen Energy*, 2022, **47**, 13561–13578.
29 X. Xu, Z. Shao and S. P. Jiang, *Energy Technol.*, 2022, **10**(11), 2200573.

30 X. Zhang, X. Wang and X. Lv, *ChemSusChem*, 2025, **18**(2), e202401663.
31 M. V. Kante, M. L. Weber, S. Ni, I. C. G. van den Bosch, E. van der Minne, L. Heymann, L. J. Falling, N. Gauquelin, M. Tsvetanova, D. M. Cunha, G. Koster, F. Gunkel, S. Nemšák, H. Hahn, L. Velasco Estrada and C. Baeumer, *ACS Nano*, 2023, **17**, 5329–5339.
32 W. Cai, X. Cao, Y. Wang, S. Chen, J. Ma and J. Zhang, *Adv. Mater.*, 2024, **36**(45), 2409949.
33 M. Anandkumar and E. Trofimov, *J. Alloys Compd.*, 2023, **960**, 170690.
34 D. Wang, Z. Liu, S. Du, Y. Zhang, H. Li, Z. Xiao, W. Chen, R. Chen, Y. Wang, Y. Zou and S. Wang, *J. Mater. Chem. A*, 2019, **7**, 24211–24216.
35 N. Vieceli, P. Benjamasutin, R. Promphan, P. Hellström, M. Paulsson and M. Petranikova, *ACS Sustainable Chem. Eng.*, 2023, **11**, 9662–9673.
36 N. Yuran, B. Muniyandi, A. Saha, S. Yochelis, D. Sharon, Y. Paltiel and M. Noked, *J. Phys. Chem. Lett.*, 2024, **15**, 2682–2689.
37 R. D. Shannon, *Acta Crystallogr., Sect. A*, 1976, **32**, 751–767.
38 B. G. Ershov, *J. Mol. Liq.*, 2023, **390**, 123129.
39 S. Bhattacharjee, M. Isegawa, M. Garcia-Ratés, F. Neese and D. A. Pantazis, *J. Chem. Theory Comput.*, 2022, **18**, 1619–1632.
40 B. B. de Menezes, L. M. Frescura, D. Schein, M. Zadra and M. B. da Rosa, *Cienc. Nat.*, 2023, **45**, e74574.
41 C. Julien, *Ionics*, 1999, **5**, 351–357.
42 C. Julien and G. A. Nazri, *Mater. Res. Soc. Symp. Proc.*, 1999, **548**, 79–90.
43 R. Nagarajan and N. Tomar, *J. Solid State Chem.*, 2009, **182**, 1283–1290.
44 N. Mattila and A. J. Karttunen, *Mater. Res. Express*, 2020, **7**, 075502.
45 H. Koga, PhD thesis, Université Sciences et Technologies, 2014.
46 J. Li, W. Zhong, Q. Deng, Q. Zhang and C. Yang, *Int. J. Extrem. Manuf.*, 2022, **4**, 042004.
47 Z. Chen, W. Zou, R. Zheng, W. Wei, W. Wei, B.-J. Ni and H. Chen, *Green Chem.*, 2021, **23**, 6538–6547.
48 B. Cui, C. Liu, J. Zhang, J. Lu, S. Liu, F. Chen, W. Zhou, G. Qian, Z. Wang, Y. Deng, Y. Chen and W. Hu, *Sci. China Mater.*, 2021, **64**, 2710–2718.
49 N. Yu, H.-J. Liu, J.-K. Ren, Z.-J. Zhang, Y. Ma, X.-J. Zhai, D.-P. Liu, Y.-M. Chai and B. Dong, *Fuel*, 2024, **357**, 129786.
50 S. Li, X. Zhu, X. Wang, W. Luo, X. Yu, Q. Guo, K. Song, H. Tian, X. Cui and J. Shi, *Mater. Chem. Front.*, 2023, **7**, 5868–5878.
51 L. Jia, G. Du, D. Han, Y. Wang, W. Zhao, S. Chen, Q. Su and B. Xu, *J. Colloid Interface Sci.*, 2024, **653**, 246–257.
52 P. Patel, D. Schwartz, X. Wang, R. Lin, O. Ajao and A. Seifitokaldani, *ACS Sustainable Chem. Eng.*, 2022, **10**, 4206–4217.
53 D. Chen, Y. Ding, X. Cao, L. Wang, H. Lee, G. Lin, W. Li, G. Ding and L. Sun, *Angew. Chem., Int. Ed.*, 2023, **62**(37), e202309478.
54 V. Vij, S. Sultan, A. M. Harzandi, A. Meena, J. N. Tiwari, W.-G. Lee, T. Yoon and K. S. Kim, *ACS Catal.*, 2017, **7**, 7196–7225.
55 L. Sun, X. Li, J. Li, Y. Zeng and S. Lu, *Energy Fuels*, 2025, **39**, 13969–13996.
56 Y. Zhai, X. Ren, B. Wang and S. (Frank) Liu, *Adv. Funct. Mater.*, 2022, **32**(47), 2207536.
57 W. Lin, Q. Deng, Q. Zhang, W. Min, H. Wang, J. Luo and C. Yang, *Chem. Eng. J.*, 2024, **496**, 153828.
58 Y. Yu, M. Pan, Z. Zhang, Z. An, Y. Wang and X. Hu, *Int. J. Hydrogen Energy*, 2023, **48**, 27679–27685.
59 Y. Liu, P. Liu, W. Qin, X. Wu and G. Yang, *Electrochim. Acta*, 2019, **297**, 623–632.